

# Direct-Current Triboelectric Nanogenerator Realized by Air Breakdown Induced Ionized Air Channel

Jianjun Luo, Liang Xu, Wei Tang, Tao Jiang, Feng Ru Fan, Yaokun Pang, Libo Chen, Yan Zhang, and Zhong Lin Wang\*

The air breakdown phenomenon is generally considered as a negative effect in previous research on triboelectric nanogenerators (TENGs), which is always accompanied by air ionization. Here, by utilizing the air breakdown induced ionized air channel, a direct-current triboelectric nanogenerator (DC-TENG) is designed for harvesting contact-separation mechanical energy. During working process, the charges first transfer from bottom to top electrodes through an external circuit in contact state, then flow back via the ionized air channel created by air breakdown in the separation process. So a unidirectional flow of electrical charges can be observed in the external circuit. With repeating contact-separation cycles, continuous pulsed DC output through the external circuit can be realized. This working mechanism was verified by real-time electrode potential monitoring, photocurrent signal detection, and controllable discharging observation. The DC-TENG can be used for directly and continuously charging an energy storage unit and/or driving electronic devices without using a bridge rectifier. Owing to its simplicity in structure, the mechanism is further applied to fabricate the first flexible DC-TENG. This research provides a significant fundamental study for DC-TENG technology and may expand its application in flexible electronics and flexible self-charging power systems.

based on the coupling effect of contact electrification and electrostatic induction, has been developed as a new energy harvesting technology for the new era – the era of internet of things, sensor networks, big data, robotics, and artificial intelligence.<sup>[4–10]</sup> So far, various modes of TENGs have already been demonstrated for harvesting different mechanical energies from environment, such as vibration,<sup>[11–13]</sup> wind,<sup>[14,15]</sup> water flow,<sup>[16,17]</sup> ocean wave,<sup>[18,19]</sup> and human motion.<sup>[20–22]</sup> To provide a manageable and regulated output for electronic devices, self-charging power systems<sup>[23–27]</sup> have been developed by hybridizing TENG and energy storage unit, where a rectification circuit is often needed because most of the reported TENGs exhibit an alternating-current (AC) output characteristic. There are also attempts to fabricate direct-current triboelectric nanogenerators (DC-TENGs) using wheel-belt structure or electric brushes to scavenge rotation energy.<sup>[28,29]</sup> However, to meet the demand of versatile application scenes ranging from large-scale

## 1. Introduction

With the increasing energy crisis and related environmental issues, searching for renewable energy sources has become mandatory for sustainable development of human civilization.<sup>[1–3]</sup> Recently, the triboelectric nanogenerator (TENG),

TENG arrays to flexible electronics, a more simple and general method for realizing DC-TENGs is required.

Air breakdown phenomenon is usually considered as a negative effect in previous research about TENG. For instance, abrupt and intermittent output decline in asymmetrical TENGs can be caused by air breakdown.<sup>[30]</sup> How to avoid air breakdown


J. Luo, Dr. L. Xu, Dr. W. Tang, Dr. T. Jiang, Y. Pang, L. Chen, Prof. Y. Zhang, Prof. Z. L. Wang  
CAS Center for Excellence in Nanoscience  
Beijing Key Laboratory of Micro-Nano Energy and Sensor  
Beijing Institute of Nanoenergy and Nanosystems  
Chinese Academy of Sciences  
Beijing 100083, P. R. China  
E-mail: zlwang@gatech.edu

J. Luo, Dr. L. Xu, Dr. W. Tang, Dr. T. Jiang, Y. Pang, L. Chen, Prof. Y. Zhang, Prof. Z. L. Wang  
School of Nanoscience and Technology  
University of Chinese Academy of Sciences  
Beijing 100049, P. R. China

Dr. F. R. Fan  
Department of Chemistry & Biochemistry  
University of California Santa Barbara  
Santa Barbara, CA 93106, USA

Prof. Y. Zhang  
School of Physics  
School of Physical Electronics  
University of Electronic Science and Technology of China  
Chengdu 610054, P. R. China

Prof. Z. L. Wang  
School of Material Science and Engineering  
Georgia Institute of Technology  
Atlanta, GA 30332, USA

 The ORCID identification number(s) for the author(s) of this article can be found under <https://doi.org/10.1002/aenm.201800889>.

DOI: 10.1002/aenm.201800889

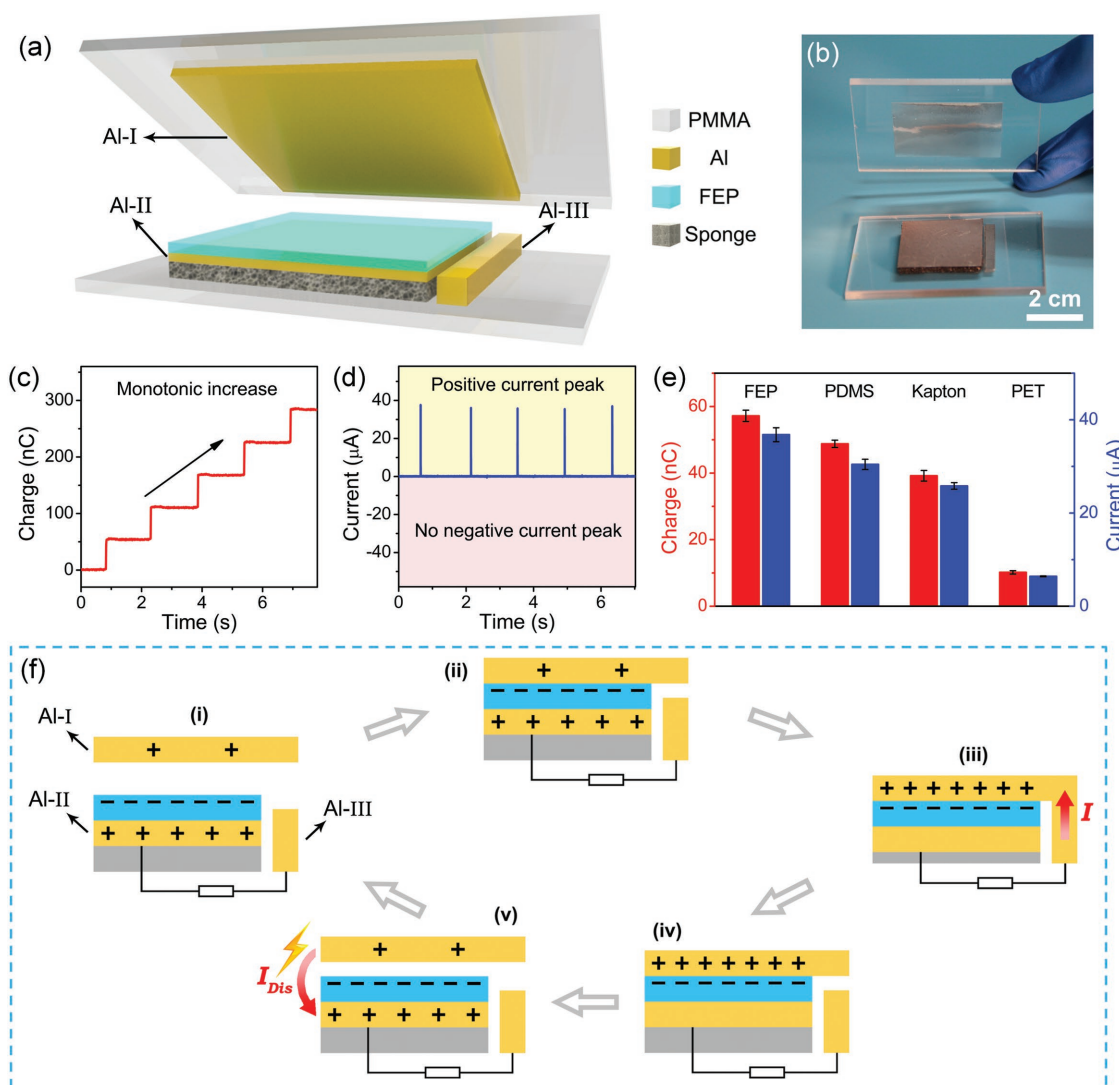


**Figure 1.** Structural design and working mechanism of the DC-TENG. a) Structure of the DC-TENG (not to scale). b) Photograph of the DC-TENG. c,d) Transferred charges and short-circuit current of the DC-TENG. e) Output performance comparison of DC-TENG using different triboelectric materials. f) Schematic illustrations showing the proposed working principle of the DC-TENG achieved through the ionized air channel caused by air breakdown.

was studied to improve the stability of TENGs. Meanwhile, since the air breakdown greatly limits the maximum retainable charge density in TENGs, high vacuum ( $\approx 10^{-6}$  torr) and different gas atmospheres were used to enhance the output power of TENG by reducing breakdown effect.<sup>[31,32]</sup>

Herein, by a novel structural design, we found that the air breakdown could be utilized for fabricating a DC-TENG with simple structure. The working mechanism of the DC-TENG is proposed and different experiments are designed to verify it. It is observed that the transferred charges via external circuit in the first half-cycle could transfer back to the original electrode through the ionized air channel caused by air breakdown, so that the charges can form a closed loop, and a continuous pulsating DC output is observed in the external circuit. Owing to its simple structure, we further fabricated a flexible DC-TENG, which could greatly expand its application in flexible electronics and self-charging power systems.

## 2. Results and Discussion

The basic structure of the DC-TENG is illustrated in **Figure 1a**. It consists of a top triboelectric aluminum (Al) electrode (noted as Al-I), a fluorinated ethylene propylene (FEP) film adhered to a back Al electrode (noted as Al-II), a sponge at the bottom as a compression layer, and an Al electrode at the bottom right corner (noted as Al-III). The photograph of the DC-TENG with an active area of  $30 \times 30 \text{ mm}^2$  is shown in **Figure 1b**. The DC-TENG was driven by a linear motor in our experiments. Details of the fabrication process and experiment setup are presented in the Experimental Section. **Figure 1c,d** shows transferred charges and short-circuit current of the DC-TENG, respectively. As can be seen, both the transferred charges and the short-circuit current show evident DC features. The transferred charges in a single cycle are about 57 nC, and the peak current reaches up to 37  $\mu\text{A}$ . **Figure S1** in the Supporting Information

shows the transferred charges of the DC-TENG in a single cycle with different active areas. It reveals that the device with larger active area provides higher output performance, while keeping similar DC output characteristic. For comparison, the output performances of the traditional AC-TENG with the same active area were measured. As shown in Figure S2 in the Supporting Information, the transferred charges of the AC-TENG in a single cycle is close to that in the DC-TENG. However, the short-circuit current shows a much smaller value, which could be explained by the shorter contact time in the DC-TENG.<sup>[33,34]</sup> Under the same stimulating conditions, the maximum peak output power of the DC-TENG reaches  $\approx 1.83$  mW, with corresponding peak current of  $\approx 30$   $\mu$ A under an external load resistance of 2 M $\Omega$  (Figure S3, Supporting Information). To further investigate the stability of the DC-TENG, periodical pressing with a frequency of 2 Hz was applied. As shown in Figure S4 in the Supporting Information, the output current only has a little decay in continuous operation of 40 000 cycles, confirming the superior stability of the DC-TENG. Using other triboelectric materials (polydimethylsiloxane (PDMS), Kapton, polyethylene terephthalate (PET)) to replace FEP, similar output characteristics can be acquired, indicating that this DC output mode can be employed universally. The output performances of the DC-TENGs constructed using various triboelectric materials are summarized in Figure 1e. Details of output measurements using different materials compared with AC-TENG can be seen in Figure S5 in the Supporting Information. The output power (FEP > PDMS > Kapton > PET) depends on the relative ability of a dielectric material to gain electrons when contacting with Al, coincident with the well-established tribo-series table.<sup>[35,36]</sup>

The working mechanism of the DC-TENG in stable working state is schematically illustrated in Figure 1f. Before entering the stable working state shown in the figure, Al-I and the FEP film get into physical contact to create triboelectric charges, with the FEP film negatively charged and Al-I positively charged according to triboelectric series. In the stable working state, the DC-generation process can be divided into four stages. In stage i, Al-I is apart from the FEP film, while negative charges is preserved on the surface of the FEP film and positive charges distribute in Al-I and Al-II. When an external force is applied onto the DC-TENG, Al-I will first contact with the FEP film, then subsequently contact and get short-circuited with Al-III through compressing the sponge (stage ii). By establishing lower potential in Al-I, the negative charges on the surface of the FEP film will induce positive charges in Al-II to transfer to Al-I through an external load and Al-III until the potential difference disappears. While the pressing force is removed, the resilience of the sponge will first make Al-I separate from Al-III but still contact with the FEP film (stage iii), as will cut off the original circuit for positive charges to transfer back from Al-I to Al-II. Thus, when separation of Al-I from the FEP film establishes a potential difference again, the positive charges still remain in Al-I. This would cause rapid increasing voltage between Al-I and Al-II in further separation, which will induce air breakdown at the side edges of the two electrodes where the electric field is more intensive due to the edge effect and the absence of FEP coverage.<sup>[37,38]</sup> Such breakdown induces an ionized air channel between these two electrodes, allowing the positive charges to transfer back partly to Al-II, as shown

in stage iv. Then the device will restore to the state depicted in stage i. In the whole process, the current in the external circuit is unidirectional, namely, DC. As long as the contact-separation motion repeats, such pulsed DC can be continuously produced in the external circuit, which makes the TENG a DC power source for external loads. According to the above mechanism, the realization of the DC output relies on two key aspects. First, in the separation process, the contact between Al-I and Al-III is cut off before the separation of Al-I and the FEP film that can cause potential difference. This structural design of the TENG ensures the charges cannot return back along the original direction. Second, while Al-I is separate from FEP, air breakdown induced by high voltage will happen, in which electrons are accelerated by the high electric field to ionize molecules in air. Then the ionized air channel is created and positive charges can be driven to transfer back from Al-I to Al-II through it. Compared with AC-TENG, DC-TENG utilize the ionized air channel to produce a continuous pulsed DC output.

To verify the working mechanism of the DC-TENG, we monitored the potential of Al-I in typical working cycle to speculate the direction of charge transfer. The measurement setup for simultaneously measuring the electrode potential and transferred charges is shown in Figure S6 in the Supporting Information. **Figure 2a** shows the real-time testing results of the DC-TENG in three typical working cycles. The potential of Al-I (blue line) can reflect the amount of reserved charges in Al-I. By matching it with the curve of charge transfer in external circuit (green line), we can speculate charge transfer events at different spots in the TENG. The enlarged view of a single cycle is shown in Figure 2b, which can be divided into four segments according to the potential characteristic of Al-I. These four segments will be discussed by combing with the aforementioned mechanism, and corresponding diagrams are inserted in Figure 2b. In segment i, when Al-I is apart from the FEP film, the potential of Al-I is about 150 V. The slight positive potential can be explained by the existence of a small amount of positive charges in Al-I. In the second segment, Al-I contacts with the FEP film. It can be seen the potential becomes negative because of the electrostatic induction of negative charges on FEP surface. While Al-I further contacts with Al-III, the lower potential on Al-I will make positive charges transfer from Al-II (grounded in the test) to Al-I via external load and Al-III. Then the potential of Al-I becomes zero (segment iii). According to the change of the  $Q-t$  curve, we can see that the charges indeed transfer through the external load in this stage. In the last segment, with the separation of Al-I, the potential first rises then decreases sharply, which should be caused by abrupt charge transfer. While the  $Q-t$  curve shows no charge transfer via external circuit in this period, the transfer most probably happens through air breakdown induced ionized air channel between Al-I and Al-II, which is also consistent with the abrupt decrease feature. When various triboelectric materials (PDMS, Kapton, PET) were used to replace FEP, similar potential peaks can be observed, illustrating the possible breakdown phenomenon is universal among different materials (Figures S7–S9, Supporting Information). Simulations of the potential distribution before and after the breakdown by COMSOL are presented in Figure 2c.

In our proposed working mechanism of the DC-TENG, air breakdown induced ionized air channel holds the key role to

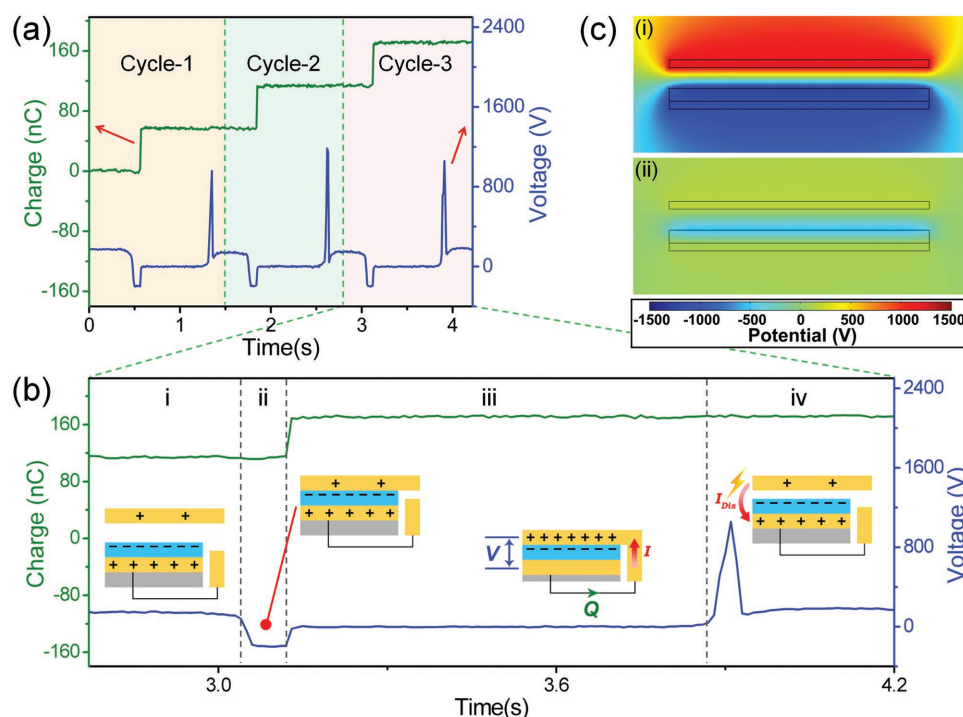


**Figure 2.** Working mechanism verification by real-time electrode potential monitoring. a) Real-time testing of electrode potential of Al-I and transferred charges between Al-II and Al-III in three cycles. The measured potential equals the voltage between Al-I and Al-II (grounded). b) Enlarged view of cycle-3 with four segments corresponding to the proposed working mechanism. c) Comparison of COMSOL simulation results before i) and after ii) the breakdown.

realize continuous DC output. To provide a more direct evidence for the air breakdown, photocurrent signals were tested using a low-dark-current photoelectric detector, as air breakdown is always accompanied by sparks. For comparison, the same test is performed on AC-TENG. **Figure 3a-i,b-i** shows the structural comparison of two different modes. Obvious light signals can be observed in **Figure 3a-ii** for DC-TENG, while no light signal has been detected in **Figure 3b-ii**. The enlarged photocurrent–time curve shows that largest width of the photocurrent peak is about 500  $\mu\text{s}$  (**Figure 3a-iii**), which accords with the duration of the ionized state produced by air breakdown.<sup>[39,40]</sup> Actually, every contact-separation cycle can be divided into two parts. For the first part (contact motion), uniform signal of charge transfer via external circuit appears for both modes of TENG. In the latter part (separation motion), instead of a reversed charge transfer signal as the AC-TENG, a photocurrent signal can be observed for the DC-TENG, without any backward charge transfer. These further prove that, for the DC-TENG, the charges transfer back through the air breakdown induced ionized air channel at the separation process of Al-I and the FEP film, unlike the AC-TENG which transfers charges back through the original external circuit. With such ionized air channel, the DC-TENG can continuously produce DC output through external load. Similarly, the photocurrent signals can also be detected when using other triboelectric materials (PDMS, Kapton, PET) to replace FEP (**Figures S11–S13**, Supporting Information).

In order to visually observe the air breakdown process, we used a high-speed camera to observe the sparks produced by air

breakdown. Here, Al-I electrode was replaced by a transparent indium tin oxide (ITO) electrode, so the sparks could be directly observed above the TENG. Video S1 in the Supporting Information shows a full working cycle of the DC-TENG. In the separation process, the breakdown point can be observed at the bottom left edge of Al-II electrode. This is consistent with our proposed mechanism that the breakdown induced ionized air channel should form between side edges of electrodes where the electric field is more intensive. By partially wrapping the side edges of Al-II electrode, the ionized air channel can be produced at specific locations, as shown in **Figure 4**. First, for comparison, we studied the TENG's working state while Al-II electrode was completely wrapped (**Figure 4a**). This results in the disappearing of previously observed DC features (**Figure 4b**), where charges no longer transfer continuously in single direction and voltage does not present any sudden decrease, implying that no air breakdown exists. Such state was confirmed by the optical images of the high-speed camera as shown in **Figure 4c** where no spark could be observed. Thus in completely wrapped situation, the air breakdown between electrodes is suppressed. Charges will transfer to the ITO electrode and remain there without any ionized air channel. Nevertheless, when partially wrapped Al-II electrode was used, the real-time testing results of electrode potential and transferred charges appeared as **Figure 2a** again, and the TENG recovered to the DC mode. The locations of the air breakdown were accurately controlled to the unwrapped point, as shown in **Figure 4d,e**, where sparks were captured precisely at the unwrapped point in working cycles. This further proves the proposed mechanism, and also

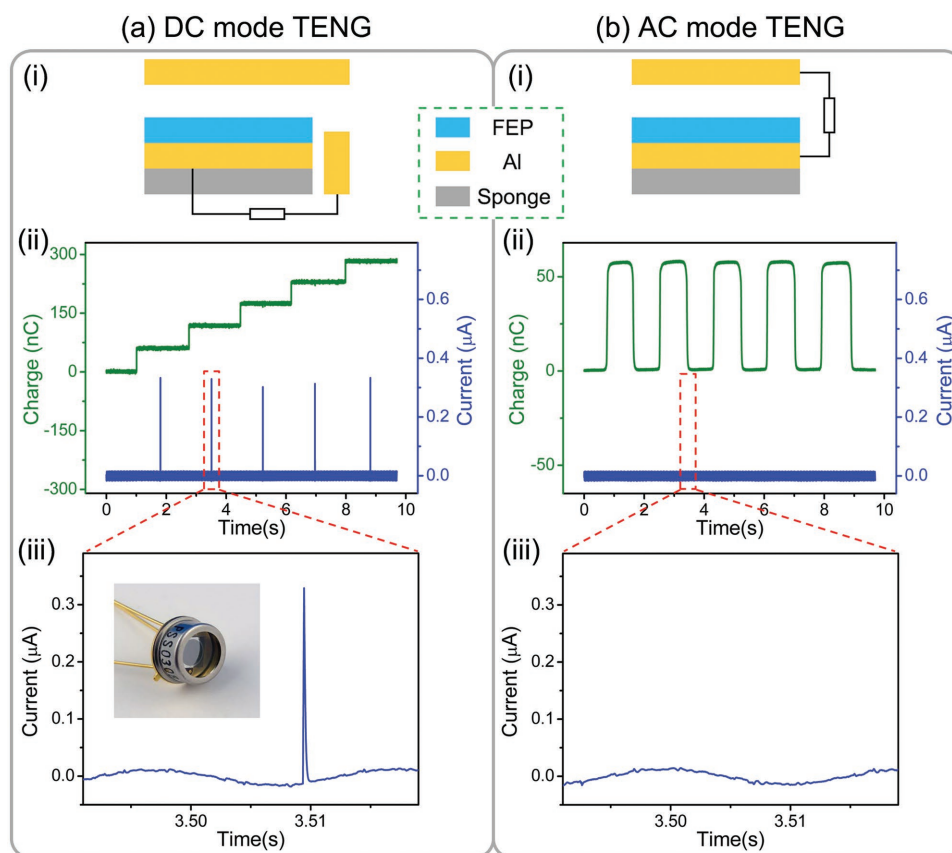


**Figure 3.** Comparison of DC-TENG and AC-TENG, and air breakdown confirmation. a) Structure of the DC-TENG i), photoelectric current detection of the DC-TENG ii), and enlarged view of the photoelectric current iii). The inset shows the photograph of the PC10-6 photoelectric detector. b) Structure of the AC-TENG i), no detectable photoelectric current signal in the AC-TENG ii,iii).

provides a method to design DC-TENG device with specific air breakdown behavior and ionized air channels.

To demonstrate the ability of the TENG as a DC power source to power electronics, a total of 160 commercial light-emitting diodes (LEDs) were used as the external load. The LEDs were divided into two groups with green and red light, respectively, and were connected to the device with opposite polarity (Figure 5a). The aforementioned TENG with an active area of  $30 \times 30 \text{ mm}^2$  and FEP as the triboelectric material was used. As illustrated in Figure 5b, the 80 green LEDs were lighted up by the TENG in contact-separation process, while no light emission can be observed from the red LEDs, indicating that the TENG has a DC output. Moreover, when the connection direction between the TENG and the LEDs was reversed (Figure 5c), only the 80 red LEDs can be lighted up, as displayed in Figure 5d. These can be also seen in Video S2 in the Supporting Information. The results indicate that the DC-TENG can be used as an efficient power source for directly and continuously driving electronic devices.

More importantly, the produced electric energy by the DC-TENG can be stored in capacitors or batteries without using a rectifier. Figure 5e shows the circuit diagram of directly charging a  $1 \mu\text{F}$  capacitor at different frequencies. The voltage of the capacitor is measured in Figure 5f, indicating that the charging rate is increased with higher working frequencies.

Compared with the previous charging method with a rectifier, the direct charging of an energy storage unit by the DC-TENG will largely improve the practicability of the TENG as a constant current source for electronics.

Owing to its simple structure, the mechanism can also be applied to fabricate flexible DC-TENGs. By simply replacing the rigid polymethyl methacrylate with flexible Kapton film, a simple structured and fully flexible DC-TENG can be fabricated. In general, many rectifiers will be needed for parallel connecting several AC-TENGs to increase the harvested power since they are not necessarily synchronized, which causes inconvenience in practical use. Here, without worrying about such problem, large amounts of flexible DC-TENG units can be integrated together to enable high-power energy harvesting. Figure 5g presents the structure of a flexible multilayered DC-TENG in different views. A  $200 \mu\text{m}$  thick Kapton thin film was selected as the substrate due to its flexibility, light weight, and proper stiffness. Through the zigzag-shaped design, four different DC-TENG units were stacked together in vertical direction with spaced intervals. As demonstrated in Figure 5h,i, the fabricated flexible multilayered DC-TENG shows great flexibility, making it appropriate for using in flexible electronics. The amount of units can be easily controlled in this zigzag-shaped DC-TENG. Figure S14a in the Supporting Information shows the circuit diagram of charging a

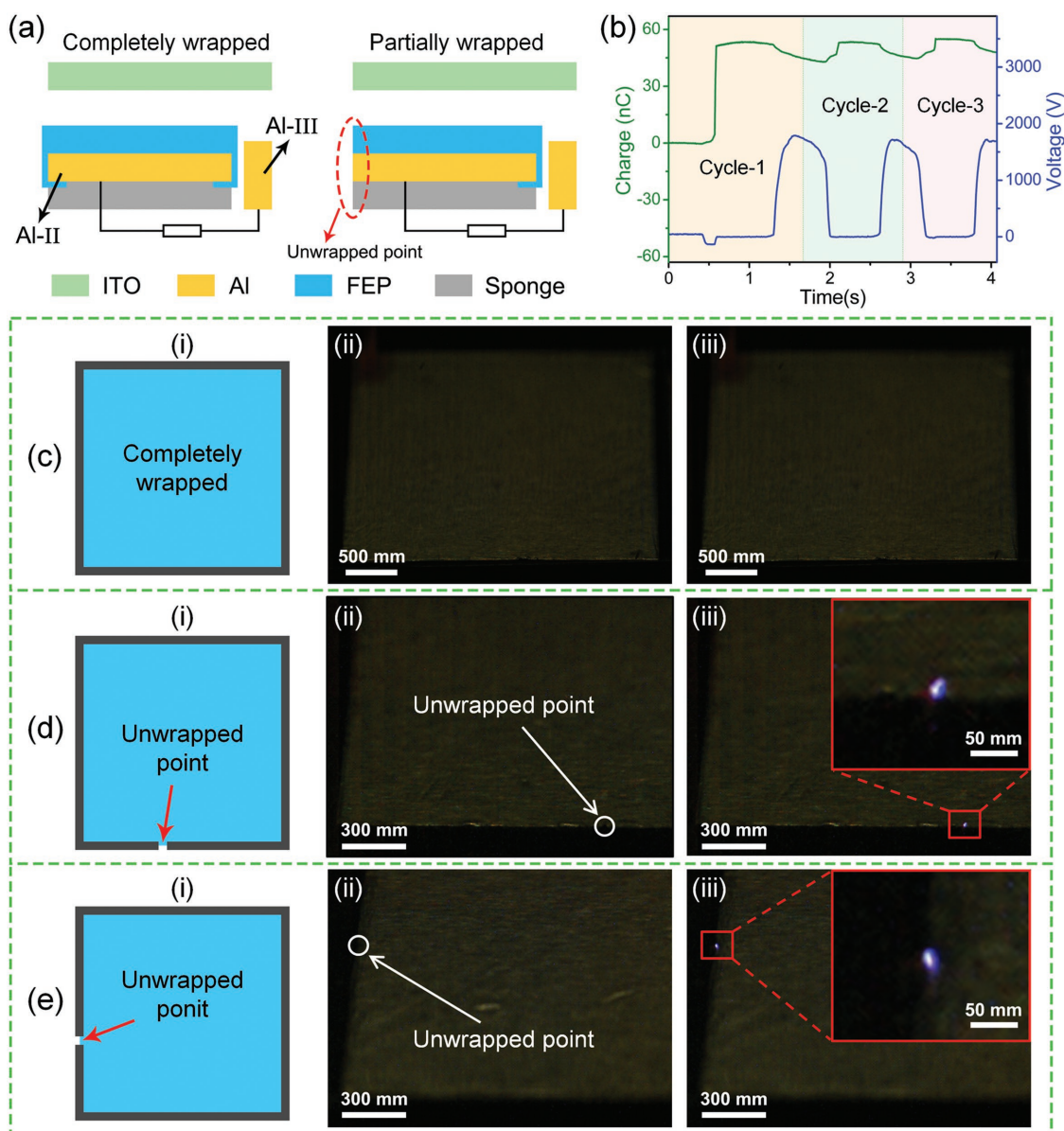


**Figure 4.** DC-TENG with a wrapped Al-II electrode. a) Schematic diagram showing TENGs with Al-II electrodes completely wrapped or partially wrapped. b) Real-time testing of electrode potential and transferred charges in three cycles when Al-II electrode was completely wrapped. Continuous DC output cannot be achieved, and no abrupt charge transfer signal can be observed. c–e) Observation of sparks using a high-speed camera. No spark can be observed when Al-II electrode was completely wrapped c). Controlled locations of air breakdown at the bottom d) and left e) side unwrapped points.

1  $\mu\text{F}$  capacitor using such DC-TENG with multiple units in parallel. Without connecting a rectifier, the capacitor can be charged successfully and the charging curves are shown in Figure S14b in the Supporting Information, which reveals that more integrated units will provide larger output charges. The flexible DC-TENG can be further integrated with the capacitor and electronic devices to form a self-powered system. Figure 5j displays that a capacitor of 1000  $\mu\text{F}$  can be charged from 0.9 to 1.37 V in about 727 s by a flexible DC-TENG with four unit numbers (charging frequency: 5 Hz). They can sustainably drive a calculator to form a self-powered system for demonstration.

### 3. Conclusion

In summary, we report here a novel design of a DC-TENG, which can convert the contact-separation mechanical energy into DC electricity without using a rectifier. The charges first transfer from bottom to top electrode through the external circuit, then flow back via the air breakdown induced ionized air channel. With repeated contact-separation cycles, continuous pulsed DC output can be produced in the external circuit. This working mechanism by utilizing air breakdown was verified by different experiments, including real-time electrode potential and transferred charges testing, photocurrent signal detection,

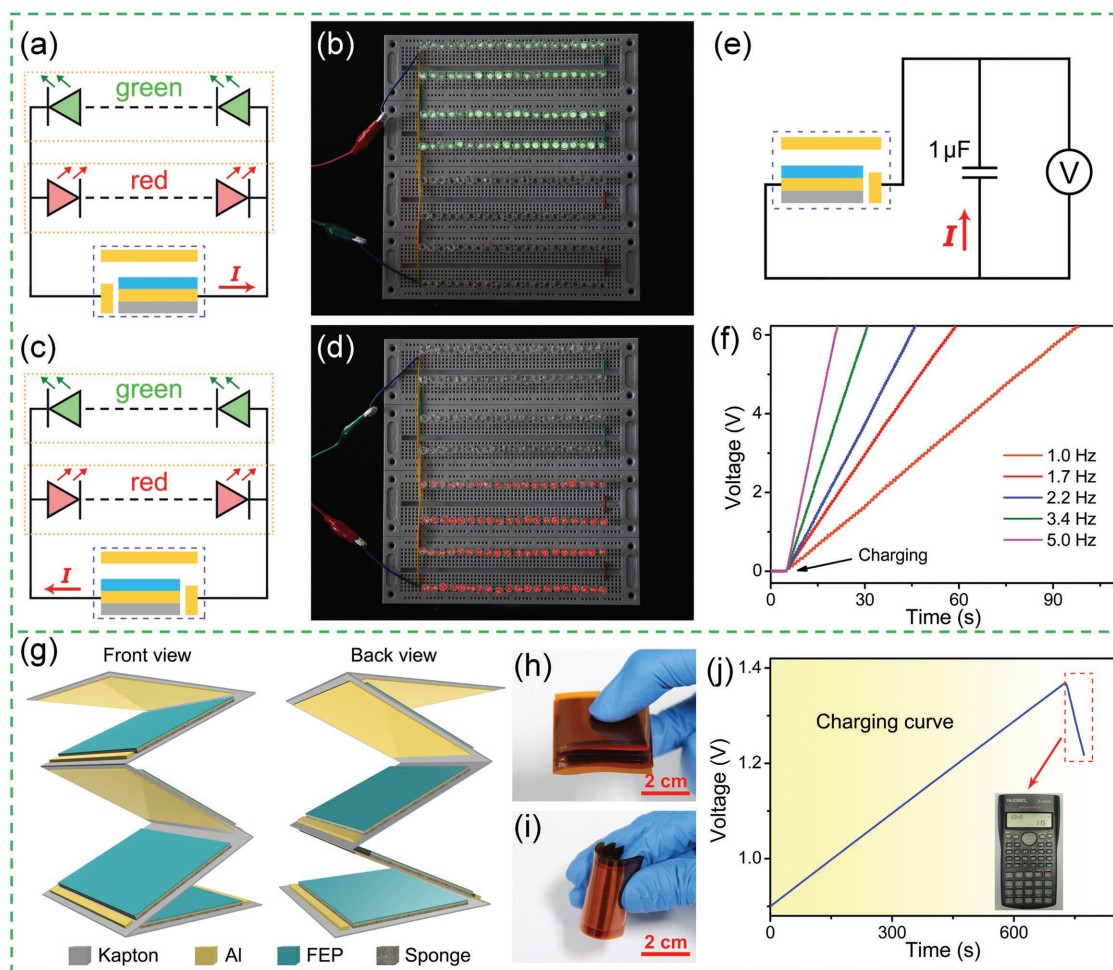


**Figure 5.** DC-TENG as a power source for electronics. a) Schematic diagram of the connection between the DC-TENG and the green and red LEDs. b) Photograph of the DC-TENG driving the green LEDs. c) Schematic diagram of the reversed connection between the DC-TENG and the green and red LEDs. d) Photograph of the red LEDs lighted up by the reversely connected DC-TENG. e) Circuit diagram for the DC-TENG to directly and continuously charge a capacitor of  $1 \mu\text{F}$  without a rectifier. f) Measured voltage of a  $1 \mu\text{F}$  capacitor charged by the DC-TENG at different frequencies. g) Zigzag-shaped structure of the flexible multilayered DC-TENG with four units (not to scale). h, i) Photographs of the flexible multilayered DC-TENG. j) Charging curve of a  $1000 \mu\text{F}$  capacitor charged by the flexible multilayered DC-TENG. The inset shows the photograph of the charged capacitor to power a calculator.

and controllable air breakdown observation. Furthermore, owing to its simplicity in structure, the mechanism is further applied to fabricate the first flexible DC-TENG. This work may open up new avenues for further fundamental research and experimental development of DC energy harvesting systems used in various scenes including large-scale energy harvesting and flexible electronics.

## 4. Experimental Section

**Fabrication of the DC-TENG:** An Al film (Al-I,  $40 \times 30 \text{ mm}^2$ ) was attached to the center of an acrylic substrate ( $70 \times 50 \text{ mm}^2$ ), acting as a triboelectric material and an electrode simultaneously. The other triboelectric material, an FEP film, was adhered to a cushioned Al film (Al-II) and then onto another acrylic substrate. A piece of sponge was placed between Al-II and its corresponding acrylic substrate. The FEP film, Al-II, and the sponge were of the same size,  $30 \times 30 \text{ mm}^2$ .

Another Al film (Al-III,  $3 \times 30 \text{ mm}^2$ ) was attached on the acrylic substrate beside the FEP film. The only difference for the fabrication of AC-TENG was the removing of Al-III. The thickness of Al and FEP films was  $50 \mu\text{m}$ , and the thickness of sponge and acrylic substrate was  $3 \text{ mm}$ . Other triboelectric materials (PDMS, Kapton, PET) to replace FEP were  $100 \mu\text{m}$  thick.

**Characterizations and Measurements:** The contact-separation process of the DC-TENG was driven by a linear motor (Linmot) for electrical measurements, with a pressing force of  $9.6 \text{ N}$  in the contact state, and a separation distance of  $10 \text{ mm}$  on the release step unless otherwise specified. A programmable electrometer (Keithley 6514) was used to test the transferred charges and short-circuit current. An electrostatic voltmeter (Monroe ME-279) was adopted to detect the potential of the top electrode. A low-dark-current photoelectric detector (First Sensor PC10-6TO5) was applied to detect the light of sparks during air breakdown. A high-speed camera (Photron FASTCAM Mini AX) was used to observe the sparks during air breakdown. All experiments were performed in the atmosphere, at room temperature and humidity of about 40%. The light signal was obtained in darkroom.

## Supporting Information

Supporting Information is available from the Wiley Online Library or from the author.

## Acknowledgements

J.L., L.X., and W.T. contributed equally to this work. The research was supported by the National Key R & D Project from Minister of Science and Technology (2016YFA0202704), the National Science Foundation (DMR-1505319), National Natural Science Foundation of China (Grant No. 51605033, 61504009, 51432005, 5151101243, 51561145021), Beijing Municipal Science & Technology Commission (Z171100000317001), Beijing Municipal Science & Technology Commission (Y3993113DF), and China Postdoctoral Science Foundation (Grant No. 2015M581041).

## Conflict of Interest

The authors declare no conflict of interest.

## Keywords

air breakdown, direct current, ionized air channel, triboelectric nanogenerators

Received: March 20, 2018

Revised: June 11, 2018

Published online:

- [1] Q. Schiermeier, J. Tollefson, T. Scully, A. Witze, O. Morton, *Nature* **2008**, *454*, 816.
- [2] D. Gielen, F. Boshell, D. Saygin, *Nat. Mater.* **2016**, *15*, 117.
- [3] N. Kittner, F. Lill, D. M. Kammen, *Nat. Energy* **2017**, *2*, 17125.
- [4] F. R. Fan, Z. Q. Tian, Z. L. Wang, *Nano Energy* **2012**, *1*, 328.
- [5] Z. L. Wang, J. Chen, L. Lin, *Energy Environ. Sci.* **2015**, *8*, 2250.
- [6] Z. L. Wang, *Mater. Today* **2017**, *20*, 74.
- [7] S. Park, H. Kim, M. Vosgueritchian, S. Cheon, H. Kim, J. H. Koo, T. R. Kim, S. Lee, G. Schwartz, H. Chang, Z. Bao, *Adv. Mater.* **2014**, *26*, 7324.
- [8] C. K. Jeong, K. M. Baek, S. Niu, T. W. Nam, Y. H. Hur, D. Y. Park, G. T. Hwang, M. Byun, Z. L. Wang, Y. S. Jung, K. J. Lee, *Nano Lett.* **2014**, *14*, 7031.
- [9] B. N. Chandrashekar, B. Deng, A. S. Smitha, Y. Chen, C. Tan, H. Zhang, H. Peng, Z. Liu, *Adv. Mater.* **2015**, *27*, 5210.
- [10] F. R. Fan, W. Tang, Z. L. Wang, *Adv. Mater.* **2016**, *28*, 4283.
- [11] J. Chen, G. Zhu, W. Yang, Q. Jing, P. Bai, Y. Yang, T. C. Hou, Z. L. Wang, *Adv. Mater.* **2013**, *25*, 6094.
- [12] W. Xu, L. B. Huang, J. Hao, *Nano Energy* **2017**, *40*, 399.
- [13] H. S. Wang, C. K. Jeong, M. H. Seo, D. J. Joe, J. H. Han, J. B. Yoon, K. J. Lee, *Nano Energy* **2017**, *35*, 415.
- [14] Y. Yang, G. Zhu, H. Zhang, J. Chen, X. Zhong, Z. H. Lin, Y. Su, P. Bai, X. Wen, Z. L. Wang, *ACS Nano* **2013**, *7*, 9461.
- [15] M. L. Seol, J. H. Woo, S. B. Jeon, D. Kim, S. J. Park, J. Hur, Y. K. Choi, *Nano Energy* **2015**, *14*, 201.
- [16] Y. Xie, S. Wang, S. Niu, L. Lin, Q. Jing, Y. u , Z. Wu, Z. L. Wang, *Nano Energy* **2014**, *6*, 129.
- [17] Q. Liang, X. Yan, X. Liao, Y. Zhang, *Nano Energy* **2016**, *25*, 18.
- [18] G. Zhu, Y. Su, P. Bai, J. Chen, Q. Jing, W. Yang, Z. L. Wang, *ACS Nano* **2014**, *8*, 6031.
- [19] L. Xu, Y. Pang, C. Zhang, T. Jiang, X. Chen, J. Luo, W. Tang, X. Cao, Z. L. Wang, *Nano Energy* **2017**, *31*, 351.
- [20] J. Luo, W. Tang, F. R. Fan, C. Liu, Y. Pang, G. Cao, Z. L. Wang, *ACS Nano* **2016**, *10*, 8078.
- [21] W. Seung, H. J. Yoon, T. Y. Kim, H. Ryu, J. Kim, J. H. Lee, J. H. Lee, S. Kim, Y. K. Park, Y. J. Park, S. W. Kim, *Adv. Energy Mater.* **2017**, *7*, 1600988.
- [22] Y. Pang, J. Li, T. Zhou, Z. Yang, J. Luo, L. Zhang, G. Dong, C. Zhang, Z. L. Wang, *Nano Energy* **2017**, *31*, 533.
- [23] X. Pu, L. Li, H. Song, C. Du, Z. Zhao, C. Jiang, G. Cao, W. Hu, Z. L. Wang, *Adv. Mater.* **2015**, *27*, 2472.
- [24] J. Luo, F. R. Fan, T. Jiang, Z. Wang, W. Tang, C. Zhang, M. Liu, G. Cao, Z. L. Wang, *Nano Res.* **2015**, *8*, 3934.
- [25] S. Niu, X. Wang, F. Yi, Y. S. Zhou, Z. L. Wang, *Nat. Commun.* **2015**, *6*, 8975.
- [26] J. Wang, Z. Wen, Y. Zi, P. Zhou, J. Lin, H. Guo, Y. Xu, Z. L. Wang, *Adv. Funct. Mater.* **2016**, *26*, 1070.
- [27] H. Guo, M.-H. Yeh, Y. C. Lai, Y. Zi, C. Wu, Z. Wen, C. Hu, Z. L. Wang, *ACS Nano* **2016**, *10*, 10580.
- [28] Y. Yang, H. Zhang, Z. L. Wang, *Adv. Funct. Mater.* **2014**, *24*, 3745.
- [29] C. Zhang, T. Zhou, W. Tang, C. Han, L. Zhang, Z. L. Wang, *Adv. Energy Mater.* **2014**, *4*, 1301798.
- [30] Z. Su, M. Han, X. Cheng, H. Chen, X. Chen, H. Zhang, *Adv. Funct. Mater.* **2016**, *26*, 5524.
- [31] J. Wang, C. Wu, Y. Dai, Z. Zhao, A. Wang, T. Zhang, Z. L. Wang, *Nat. Commun.* **2017**, *8*, 88.
- [32] Y. Zi, C. Wu, W. Ding, Z. L. Wang, *Adv. Funct. Mater.* **2017**, *27*, 1700049.
- [33] G. Cheng, Z. H. Lin, L. Lin, Z. I. Du, Z. L. Wang, *ACS Nano* **2013**, *7*, 7383.
- [34] R. D. I. G. Dharmasena, K. D. G. I. Jayawardena, C. A. Mills, J. H. B. Deane, J. V. Anguita, R. A. Dorey, S. R. P. Silva, *Energy Environ. Sci.* **2017**, *10*, 1801.
- [35] D. K. Davies, *J. Phys. D: Appl. Phys.* **1969**, *2*, 1533.
- [36] A. F. Diaz, R. M. Felix-Navarro, *J. Electrostat.* **2004**, *62*, 277.
- [37] S. Niu, Y. Liu, S. Wang, L. Lin, Y. S. Zhou, Y. Hu, Z. L. Wang, *Adv. Funct. Mater.* **2014**, *24*, 3332.
- [38] Y. Zi, S. Niu, J. Wang, Z. Wen, W. Tang, Z. L. Wang, *Nat. Commun.* **2015**, *6*, 8376.
- [39] M. M. Pejovic, G. S. Ristic, J. P. Karamarkovic, *J. Phys. D: Appl. Phys.* **2002**, *35*, R91.
- [40] W. Zhang, T. S. Fisher, S. V. Garimella, *J. Appl. Phys.* **2004**, *96*, 6066.